Performance enhancement of multiple-mode FBMC-IM VLC systems with group-interleaved precoding

Hong Wen, ¹ D Hao Chen, ¹ Qinghui Chen, ^{1,3} D Kexiong Liu, ¹ Chen Chen, ^{2,4} D and Dalong Mo¹

Abstract: In this paper, we introduce the application of multiple-mode index modulation (MMIM) to filter bank multi-carrier (FBMC) for the first time in visible light communication (VLC) systems. Additionally, we propose a group-interleaved precoding (GIP) technique to enhance the performance of MM-FBMC-IM-based VLC systems. The GIP technique reduces complexity in precoding by grouping and achieves equalization of the signal-to-noise ratio (SNR) through subcarrier interleaving. Furthermore, we develop a robust low-complexity maximum likelihood (LCML) detector, which can maintain the same computational complexity as a conventional LCML detector and achieve similar performance as an ML detector. The effectiveness and superiority of the proposed MM-FBMC-IM-based VLC system with GIP are demonstrated through comprehensive validation by both simulation and experimental results.

© 2024 Optica Publishing Group under the terms of the Optica Open Access Publishing Agreement

1. Introduction

Due to its unique advantages, visible light communication (VLC) has garnered considerable attention as a contender for 6G communication. These include the integration of illumination and communication, freedom from spectrum licensing, and its resilience to electromagnetic interference [1,2]. Unlike conventional laser communications, VLC offers a wide range of flexible wireless access capabilities, making it suitable for diverse applications such as indoor positioning, intelligent transportation, and industrial Internet of Things (IoT) [3–5]. Due to their stability and cost-effectiveness, light-emitting diodes (LEDs) are commonly used as signal transmitters in VLC systems. However, LEDs suffer from an inherent challenge in terms of modulation bandwidth. Recent advancements have addressed the limitations of LED-based VLC systems, such as orthogonal frequency division multiplexing (OFDM), non-orthogonal multiple access (NOMA), and filter bank multicarrier (FBMC) [6–8]. Different from OFDM, FBMC offers significant benefits, including the ability to handle inter-symbol interference (ISI) without the need for a cyclic prefix (CP), resulting in improved modulation bandwidth and robustness to high out-of-band (OOB) emission in VLC systems [9,10].

Recently, index modulation (IM) has been suggested as a competitive digital modulation technique for wireless communication [11]. IM enhances the transmit power of active subcarriers and conveys additional information bits by subcarrier activation to compensate for the signal constellation's size. Consequently, OFDM with IM outperforms classical OFDM in terms of bit error rate (BER). The application of IM technology also extends to emerging systems including FBMC-IM [12]. Nonetheless, a limitation of OFDM/FBMC-IM is that inactive subcarriers cannot transmit information bits. In response, dual-mode (DM) and multiple-mode (MM) OFDM-IM have been proposed as an enhanced version of OFDM-IM [13,14]. They

¹College of Computer Science, Hunan University of Technology, Zhuzhou 412007, China

²School of Microelectronics and Communication Engineering, Chongqing University, Chongqing 400044, China

³qhchen@hut.edu.cn

⁴c.chen@cqu.edu.cn

activate all subcarriers carrying data, which enables the transmission of symbols with diverse constellations. This improvement substantially increases the spectral efficiency (SE). Moreover, research has demonstrated that MM-OFDM-IM outperforms traditional DM-OFDM-IM in overall performance [15].

The imperfect frequency response of the VLC system, combined with interferences, leads to significant fluctuations in the signal-to-noise ratio (SNR) over the subcarriers. Such non-uniform SNR distribution can result in poor BER performance at the receiver. Precoding is widely recognized as an effective solution to equalize the SNR of different subcarriers and mitigate the impact of frequency-selective fading [16]. In [17], the discrete Fourier transform (DFT) spreading was applied to DM-OFDM-IM, leading to effective suppression of frequency selective fading. Subsequently, the use of the orthogonal circular matrix transform (OCT) in DM-OFDM-IM has been shown to outperform DFT spreading [18]. In [19], a precoded FBMC-IM system was proposed to enhance the SE of multicarrier systems. However, all of these aforementioned systems utilize conventional full data-carrying subcarrier precoding (FDSP). To further enhance and evolve precoding techniques, partial data-carrying subcarriers precoding (PDSP) was introduced to decrease the complexity of precoding implementation [20]. However, the PDSP provides minimal reduction in complexity and does not improve performance improvements compared to the FDSP.

In this paper, we applied the multiple-mode index modulation (MMIM) to FBMC for the first time, and proposed a novel group-interleaved precoding (GIP) scheme to enhance the performance of MM-FBMC-IM-based VLC systems. The GIP scheme, with its complexity reduction and performance improvement, varies depending on the number of groups. Furthermore, we introduced a robust low-complexity maximum likelihood (LCML) detector for MMIM symbol detection.

2. Principle of GIP-MM-FBMC-IM

2.1. Multiple-mode FBMC-IM

Figure 1 depicts the schematic diagram of the transceiver structure of the MM-FBMC-IM system with GIP precoding. The MM-FBMC-IM system consists of N_d available subcarriers that are divided into B subblocks. Each subblock contains $N = N_d/B$ subcarriers. For the purpose of explanation, let's consider the b-th subblock, where $b \in \{1, \ldots, B\}$. Within the b-th subblock, the input P bits are divided into two parts: 1) P_I index bits are fed into the index selector to determine the order of the modes $\{S_i^1, \ldots, S_i^N\}$ to be employed by the N-th subcarriers; 2) $\sum_{n=1}^N P_n$ symbol bits are sent to the constellation mapper to generate complex-valued symbols, where P_n is the number of symbol bits carried on the n-th subcarrier. In addition, the $\sum_{n=1}^N P_n$ symbol bits are mapped by constellation mapper $\mathcal{M}_n = [S_1^n, S_2^n, \ldots, S_{M_n}^n]$, where \mathcal{M}_n represents a M_n -Phase Shift Keying (PSK) modulation. After that, these obtained subblocks are sent to a FBMC block creator to be concatenated into an MM-FBMC-IM symbol x, which is expressed as

$$\boldsymbol{x} = [x_1, x_2, \dots, x_{N_d}]^T = [s_1^{(1)}, \dots, s_N^{(1)}, s_1^{(2)}, \dots, s_N^{(2)}, \dots, s_1^{(B)}, \dots, s_N^{(B)}]^T$$
 (1)

The constellation point design follows the same approach as described in [15], which aims to maximize the minimum inter-mode distance (MIRD) and minimum intra-mode distance (MIAD). To ensure that the mapped symbols in each subblock are modulated with equal probability across the 4 modes of constellations, the mapping table of MM-FBMC-IM is provided in Table 1.

2.2. Group-interleaved precoding

After performing MMIM, the total number of data-carrying subcarriers N_d is interleaved into G groups, where each group contains $L = N_d/G$ subcarriers. Therefore, the symbols of the g-th group are denoted as $f^{(g)} = [x_g, x_{g+G}, x_{g+(L-1)G}]^T$, where $g \in \{1, \ldots, G\}$. Then, each group of

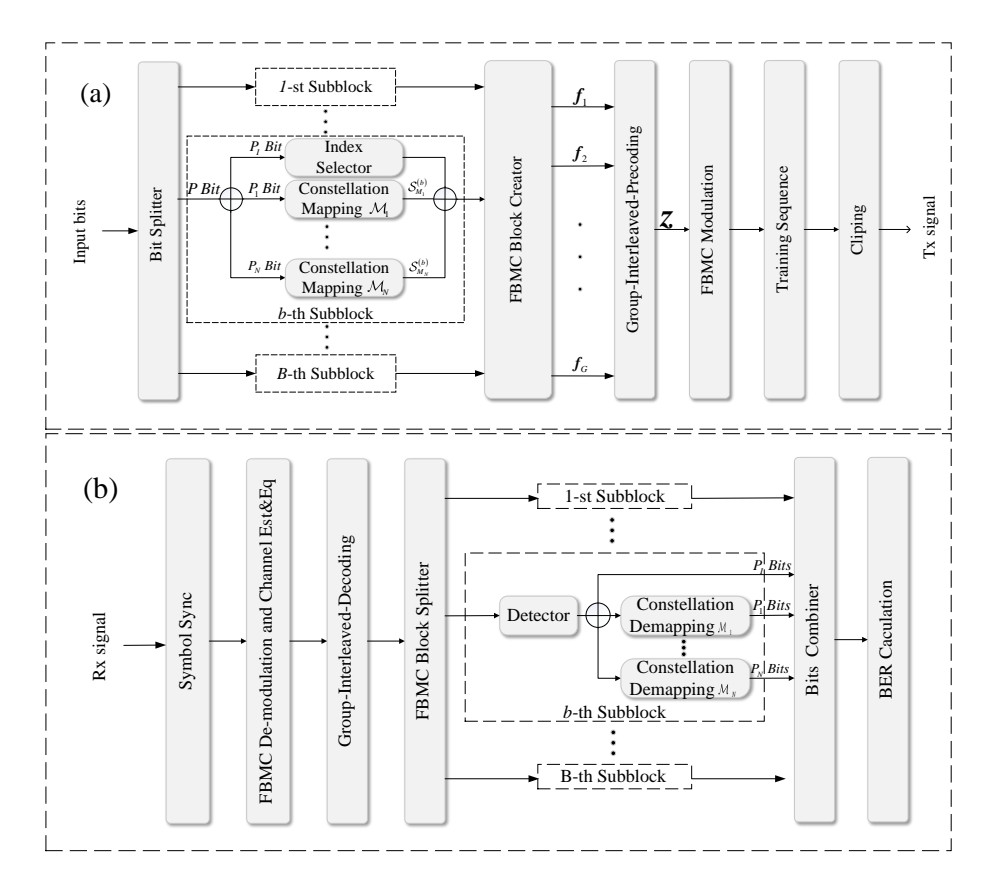


Fig. 1. Block diagrams of GIP-MM-FBMC-IM: (a) transmitter, and (b) receiver.

Table 1. The mapping table of MMIM with N=4 and $P_I=2$

Index Bits	Index set for \mathcal{M}_n	Subblocks
0,0	[1,2,3,4]	$[\mathcal{S}_i^1, \mathcal{S}_i^2, \mathcal{S}_i^3, \mathcal{S}_i^4]$
0,1	[2,3,4,1]	$[\mathcal{S}_i^2,\mathcal{S}_i^3,\mathcal{S}_i^4,\mathcal{S}_i^1]$
1,0	[3,4,1,2]	$[\mathcal{S}_i^3,\mathcal{S}_i^4,\mathcal{S}_i^1,\mathcal{S}_i^2]$
1,1	[4,1,2,3]	$[\mathcal{S}_i^4,\mathcal{S}_i^1,\mathcal{S}_i^2,\mathcal{S}_i^3]$

symbols is individually input to a precoder to implement GIP precoding. By multiplying the $L \times 1$ dimensional input symbol $f^{(g)}$ with the $L \times L$ dimensional precoding matrix C, the precoded symbol of the g-th group $z^{(g)}$ is obtained as

$$z^{(g)} = [z_1^{(g)}, z_2^{(g)}, \dots, z_L^{(g)}]^T = C f^{(g)}$$

$$= \frac{1}{\sqrt{L}} \left[\sum_{l=1}^{L} c_{1,l} \cdot x_{g+(l-1)G}, \sum_{l=1}^{L} c_{2,l} \cdot x_{g+(l-1)G}, \dots, \sum_{l=1}^{L} c_{L,l} \cdot x_{g+(l-1)G} \right]^T$$
(2)

where $c_{k,l}$ is the k-th row and l-th column element of matrix C. Next, all G group precoded symbols are interleaved and consolidated into a single GIP precoded symbol z, which can be expressed as

$$z = [z_{1}^{(1)}, z_{1}^{(2)}, \dots, z_{1}^{(G)}, z_{2}^{(1)}, z_{2}^{(2)}, \dots, z_{2}^{(G)}, \dots, z_{L}^{(1)}, z_{L}^{(2)}, \dots, z_{L}^{(G)}]^{T}
= \left[\sum_{l=1}^{L} c_{1,l} \cdot x_{1+(l-1)G}, \sum_{l=1}^{L} c_{1,l} \cdot x_{2+(l-1)G}, \dots, \sum_{l=1}^{L} c_{1,l} \cdot x_{G+(l-1)G}, \dots, \sum_{l=1}^{L} c_{2,l} \cdot x_{1+(l-1)G}, \sum_{l=1}^{L} c_{2,l} \cdot x_{2+(l-1)G}, \dots, \sum_{l=1}^{L} c_{2,l} \cdot x_{G+(l-1)G}, \dots, \sum_{l=1}^{L} c_{L,l} \cdot x_{1+(l-1)G}, \sum_{l=1}^{L} c_{L,l} \cdot x_{2+(l-1)G}, \dots, \sum_{l=1}^{L} c_{L,l} \cdot x_{G+(l-1)G} \right]^{T}.$$
(3)

As observed from Eq. (3), each symbol of z is obtained by precoding symbols from corresponding position indices in x. This shows that the precoding process in GIP preserves the original order of MM-IM symbols from x to z. For each complex-valued multiplication operation, two multipliers and one adder are required. Consequently, GIP requires a total of $4N_d^2/G$ multipliers and $4N_d^2/G - 2N_d$ adders. On the other hand, FDSP is considered to be a special case of GIP with G = 1, thus requiring a total of $4N_d^2$ multipliers and $4N_d^2 - 2N_d$ adders. In summary, the computational complexity of GIP is about 1/G of that of FDSP. Furthermore, GIP does not introduce any increase in time complexity compared to FDSP. The computational complexities of each scheme are presented in Table 2.

Table 2. The computational complexities of each scheme

Scheme	Multiplication complexity	Addition complexity
FDSP	$4 \times N_d^2$	$4 \times N_d^2 - 2 \times N_d$
GIP	$\frac{4\times N_d^2}{G}$	$4 \times \frac{N_d^2}{G} - 2 \times N_d$

At the receiver, after channel equalization and decoding, the frequency domain noise vector of the g-th group subcarriers can be represented as [20]

$$\tilde{\mathbf{N}}^{(g)} = C^{-1}(H^{(g)})^{-1} \mathbf{N}^{(g)} = \frac{1}{\sqrt{L}} \left[\sum_{i=1}^{L} \frac{n_i^{(g)}}{h_i^{(g)}} c_{i,1}^*, \sum_{i=1}^{L} \frac{n_i^{(g)}}{h_i^{(g)}} c_{i,2}^*, \dots, \sum_{i=1}^{L} \frac{n_i^{(g)}}{h_i^{(g)}} c_{i,L}^* \right]^T$$
(4)

where $H^{(g)} = diag\left\{h_1^{(g)}, h_2^{(g)}, \ldots, h_L^{(g)}\right\}$ denotes the diagonal matrix of the channel response and $N^{(g)} = \left[n_1^{(g)}, n_2^{(g)}, \ldots, n_L^{(g)}\right]^T$ represents the additive Gaussian white noise (AWGN) vector. Here, C^{-1} is the inverse of the precoding matrix and is equal to its conjugate transpose $C^H = (C^*)^T$. Based on Eq. (4), it can be deduced that the frequency domain noise is equalized to a uniform

level on each subcarrier of the *g*-th group, since $|c_{i,j}|^2 = 1$, and $\tilde{n} \sim \mathcal{NC}(0, \tilde{\sigma}^2)$, where $\tilde{\sigma}^2 = \delta^2/L \cdot \sum_{i=1}^L 1/|h_i|^2$. As a result, precoding makes it possible to achieve a consistent SNR profile across subcarriers. Considering the normalization of the transmitted symbol \boldsymbol{x} , the SNR of the *l*-th subcarrier of the *g*-th group can be obtained by

$$SNR_{l}^{(g)} = \frac{L}{\sigma^{2} \sum_{i=1}^{L} 1/\left|h_{i}^{(g)}\right|^{2}}$$
 (5)

Figure 2 illustrates the distinction in SNR equalization between FDSP and GIP, where G=4 and $N_d=12$. As depicted in Fig. 2(a), for the FDSP, the SNRs of all subcarriers are equalized to a uniform level. Conversely, in the case of GIP, only the SNRs of the subcarriers within each group are equalized to the same level. In addition, Fig. 2(b) shows slight variations in the equalized SNRs between different groups for the GIP. Fortunately, the deviation of the SNR between adjacent subcarriers is minimal, which effectively avoids low equalized SNRs in certain groups after GIP precoding. Due to the varying SNR balance of data-carrying subcarriers in each scheme, varying BER performances will be observed. These performance differences will be verified in the following experiments.

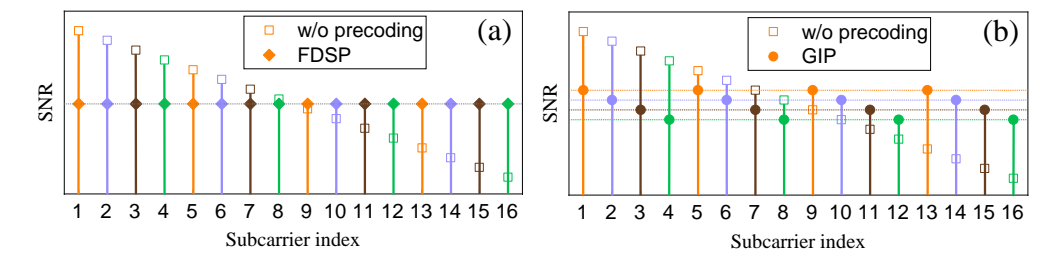


Fig. 2. SNR distribution on subcarriers with different schemes: (a) FDSP, and (b) GIP.

2.3. Low-complexity ML detector

LCML detector significantly reduces complexity compared to ML detector [21]. However, the conventional LCML detector introduces $\left(\sum_{n=1}^{N} M_n\right)^N$ potential mapping paths for each subblock, but there are only N mapping paths in MMIM, actually. In this section, we proposed a robust LCML detector designed to successfully circumvent illegal paths, thereby delivering near-optimal BER performance for GIP-MM-FBMC-IM.

The detailed procedure is summarized in Algorithm 1. For each subblock, by considering a joint detection for the individual active subcarriers and the modulated symbols carried on, the minimum distance $d_{n,\mathcal{M}_i,\varphi_n}^{(b)}$ between $y_n^{(b)}$ and \mathcal{S} that has undergone the same channel fading is given by Eq. (6). This means that the φ_n -th constellation point in \mathcal{M}_i is the mapping constellation point with the minimum probability of misjudgment for the symbols carried by the subcarrier.

Subsequently, unlike the conventional LCML detector, which directly returns \mathcal{M}_i and φ'_n for individual detection of each subcarrier's mapping detection, the proposed robust LCML detector will undergo the following additional procedures. Based on Eq. (7), the detector identifies that the symbol with the minimum probability of misjudgment in the b-th subblock is conveyed by the n'-th subcarrier and mapped by the φ'_n -th constellation point in \mathcal{M}_i . Once the mapping constellation of one subcarrier is established, the corresponding constellations of the remaining N-1 subcarriers can be derived because the constellation mapping of all subcarriers in the subcarrier block does not intersect. Notably, the improved LCML detector eliminates illegal demapping paths, and maintains the same computational complexity as the conventional LCML.

Algorithm 1. Proposed LCML detector for MM-OFDM-IM

- 1: Input: the set of the total signal points of the constellation $S = [M_1, M_2, ..., M_N]$, received symbol y and corresponding channel response h
- 2: for b = 1 : B
- 3: for n = 1 : N

$$d_{n,\mathcal{M}_i,\varphi_n}^{(b)} = \arg\min \left| y_n^{(b)} - h_{(b-1)\times N+n} \times \mathcal{S} \right|^2$$

4: if
$$n = 1$$
 or $\lambda_{n',\mathcal{M}_i,\varphi_n'}^{(b)} > d_{n,\mathcal{M}_i,\varphi_n}^{(b)}$

$$\lambda_{n',\mathcal{M}_i,\varphi_n'}^{(b)} = d_{n,\mathcal{M}_i,\varphi_n}^{(b)}, [n',\mathcal{M}_i',\varphi'] = [n,\mathcal{M}_i,\varphi_n]$$

- 5: end if
- 6: end for
- 7: return $[n', \mathcal{M}_i', \varphi']$, where $n', \mathcal{M}_i', \varphi'$ are the index of subcarrier, constellation mapper, and index of the constellation point, respectively.
- 8: end for

3. Results and discussion

The number of the FFT size and the data subcarriers with double oversampling of each GIP-MM-FBMC-IM symbol are set to 256 and 240, respectively. Furthermore, the relationship between the overlap factor of oversampling and the frequency domain parameters of the prototype filter bank's tap coefficient H is depicted in [10]. For modulation constellations, we adhere to the mapping relationship outlined in Table 1 and set $[M_1, M_2, M_3, M_4]$ to [4, 4, 2, 2], respectively. The specific constellation points are detailed in [15].

3.1. Simulation results

In the simulation, the received signal is obtained by the convolution of the transmit signal with a 20 taps channel impulse response (CIR) [18]. Subsequently, additive white Gaussian noise (AWGN) is added to the received signal. Both FDSP-MM-FBMC-IM and GIP-MM-FBMC-IM employ OCT precoding matrices. Figure 3 shows the simulation results depicting the relationship between BER and SNR for MM-FBMC-IM using various precoding schemes with an overlap factor of k = 4. With a hard decision forward error correction (HD-FEC) limitation of $BER = 3.8 \times 10^{-3}$, the FDSP provides a 2.6 dB SNR gain for the MM-FBMC-IM. Furthermore, it is observable that the performance of the GIP-MM-FBMC-IM changes with varying G. The grouping started with G = 2, and the GIP-MM-FBMC-IM exhibits its optimal performance at G = 4. As G increases, the performance of the system gradually decreases. Compared with the FDSP-MM-FBMC-IM, the GIP-MM-FBMC-IM with G = 4 achieves a 0.8 dB improvement BER while reducing precoding complexity by a substantial 75%. As G reaches 30, GIP reduces precoding complexity by 96.7% while still maintaining performance equal to FDSP. In summary, the GIP-MM-FBMC-IM effectively strikes a balance between complexity and BER performance. It's noteworthy that the MM-FBMC-IM symbols considered consist of only 120 data-carrying subcarriers in this paper. In scenarios with a greater number of data-carrying subcarriers, optimizing GIP-MM-FBMC-IM for further complexity reduction can be achieved by increasing the value of G.

To delve deeper into the reasons behind the superior performance of GIP compared to FDSP, we presented partial spectra of FDSP-MM-FBMC-IM and GIP-MM-FBMC-IM with G=4 in Fig. 3. The sunken part represents the null subcarriers and the part signal power at this position originates from the sidelobes of the signal. The power of FDSP-MM-FBMC-IM at

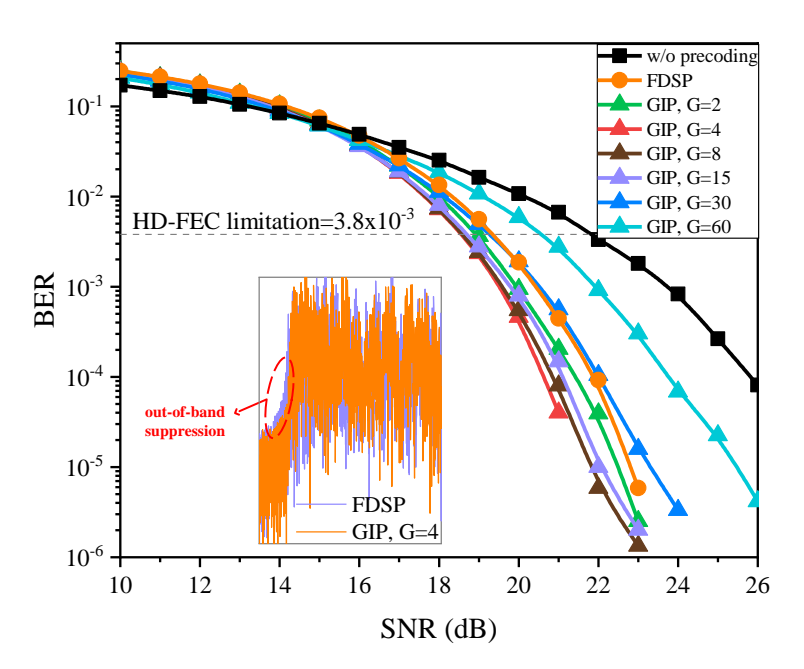


Fig. 3. BER performance comparison of MM-FBMC-IM without precoding, with FDSP, and with GIP. Insets are the electrical spectra of the FDSP-MM-FBMC-IM and GIP-MM-FBMC-IM with G = 4.

this position is marginally higher than that of GIP-MM-FBMC-IM with G=4. Consequently, GIP-MM-FBMC-IM with G=4 demonstrates enhanced out-of-band suppression capability in comparison to FDSP-MM-FBMC-IM, contributing to the smaller signal sidelobes and slightly superior performance of GIP over FDSP. When G becomes excessively large, the equalization of subcarrier SNR becomes less effective compared to schemes with smaller G. As G increases, an increasing number of subcarriers with low SNR emerge in the system, negatively impacting the error rate performance until G=30 when the performance of GIP aligns with that of FDSP.

Figure 4 illustrates the BER performance of the proposed robust LCML detector, ML detector, and conventional LCML detector for MM-FBMC-IM without precoding and GIP-MM-FBMC-IM with OCT. In MM-FBMC-IM without precoding, BER reaches the HD-FEC limitation at SNRs of 20.8 dB, 21.7 dB, and 25.3 dB for ML, proposed LCML, and conventional LCML detectors, respectively. The conventional LCML detector lags due to numerous illegal paths, while the proposed detector maintains an acceptable 0.9 dB performance gap compared to ML detectors. As SNR increases, this performance gap gradually diminishes until the proposed detector and ML detector exhibit similar performance levels. For GIP-MM-FBMC-IM, it becomes evident that GIP significantly reduces the performance gap among detectors. At the HD-FEC limitation, GIP improves performance by 2.6 dB, 3.5 dB, and 3.1 dB for ML detector, proposed LCML detector, and conventional LCML detector, respectively. This allows the proposed detector to match the BER performance of the ML detector at the HD-FEC limitation, making it the optimal solution for this system.

3.2. Experimental results

Figure 5 illustrates the experimental setup of the MM-FBMC-IM VLC system using GIP technique. At the transmitter, the conversion of pseudo-random binary sequence (PRBS) into the digital GIP-MM-FBMC-IM signal is executed through digital signal processing (DSP) in MATLAB. Then, the GIP-MM-FBMC-IM signal is loaded into an arbitrary waveform generator

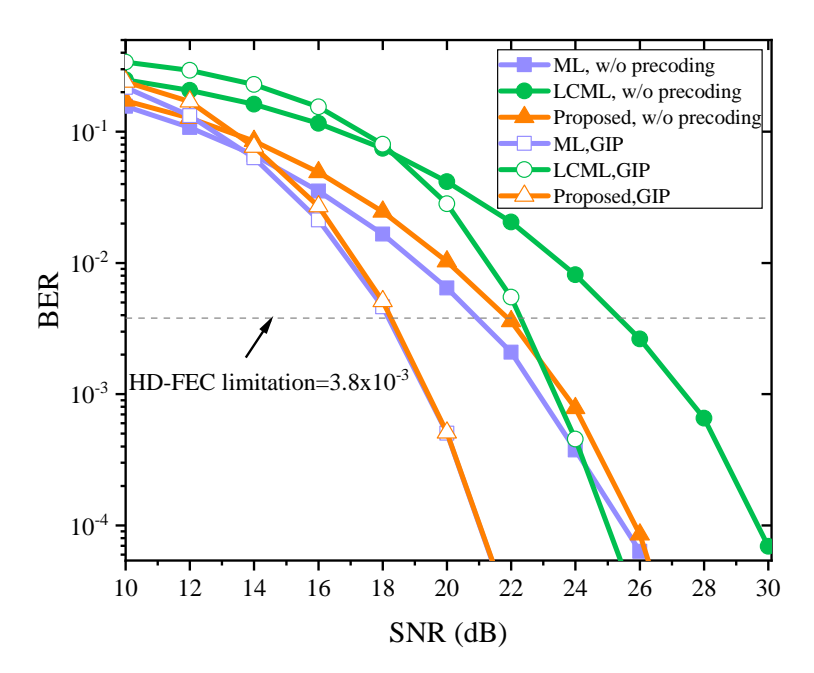


Fig. 4. BER performance of different receiver detectors in MM-FBMC-IM without precoding and GIP-MM-FBMC-IM with OCT precoding.

(AWG, AWG5200) and converted to an analog signal by a 14-bit digital-to-analog converter (DAC). In addition, the maximum sampling rate of AWG is 5.2GSa/s. After low-pass filtering (LPF), the GIP-MM-FBMC-IM analog signal is added with a direct current (DC) by the bias-tee. Subsequently, the GIP-MM-FBMC-IM electrical signal drives a blue LED (HCCLS2021CHI03) to be converted into an optical signal. This high-speed LED has a bandwidth of 90 MHz with a -3dB cutoff frequency. Finally, after being collimated by the planoconvex lens, the optical signal emitted by the LED is transmitted through free space.

At the receiver, the optical signal is detected by a photodetector (PD, S10784) after being collected by a planoconvex lens. Then the signal is amplified by a mixed-gain electrical amplifier (EA). Following amplification, the recovered electrical signal enters a digital storage oscilloscope (DSO, Keysight DSOX6004A). The DSO is equipped with a 10-bit analog-to-digital converter (ADC). In addition, the sampling rate of the DSO is 20 GSa/s. Finally, the GIP-MM-FBMC-IM digital signal is uploaded to a computer for further DSP. The electrical spectra of GIP-MM-FBMC-IM signal at transmitter and receiver are shown in Figs. 3(a) and (b), respectively.

Figure 6 shows the BER versus transmission distance for various schemes at a sampling rate of 400 MSa/s.In Fig. 6(a), with an overlap factor of k=4, the MM-FBMC-IM without precoding fails to reach the HD-FEC limitation, while the precoded MM-FBMC-IM achieves it under 90 cm. At the transmission distance less than 90cm, the GIP-MM-FBMC-IM with G=30 demonstrates comparable BER performance to that of the FDSP-MM-FBMC-IM. Notably, the GIP-MM-FBMC-IM with G=4 achieves significant distance extensions of over 50% and 16% compared to the MM-FBMC-IM without precoding and the FDSP-MM-FBMC-IM, respectively. In Fig. 6(b), with an overlap factor of k=2, the FDSP-MM-FBMC-IM with DFT maintains a BER of 3×10^{-3} after the transmission distance reaches 70 cm, with no further reduction as the transmission distance decreases. This is attributed to the weaker resistance to out-of-band attenuation in DFT-precoded FBMC systems with a low overlap factor compared to Fig. 6(a).

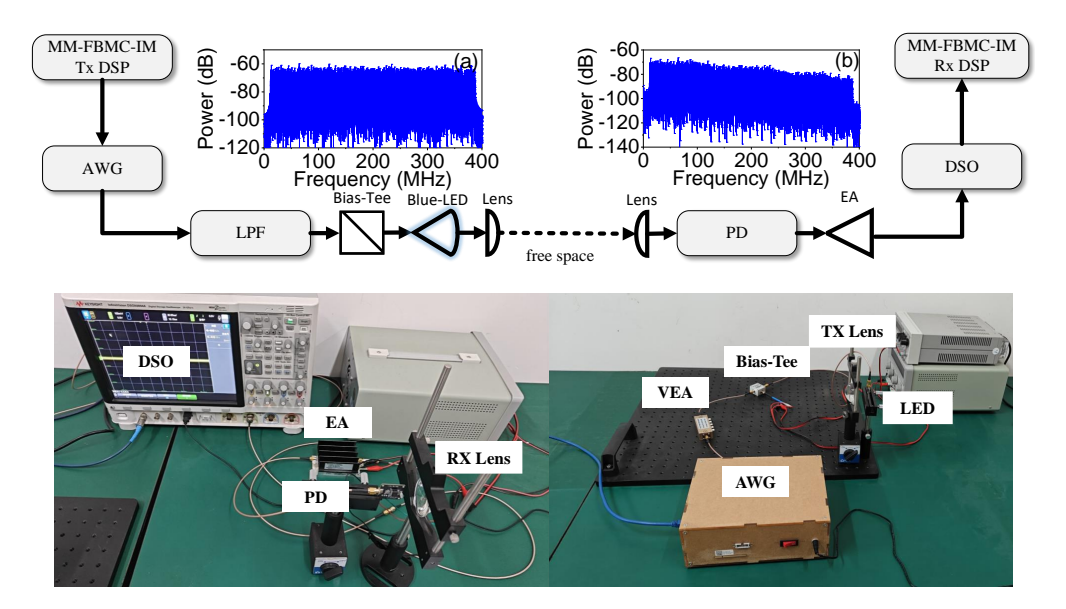


Fig. 5. Experimental setup of the MM-FBMC-IM VLC system. Insets are the electrical spectra of the GIP-MM-FBMC-IM signal at (a) the transmitter and (b) the receiver.

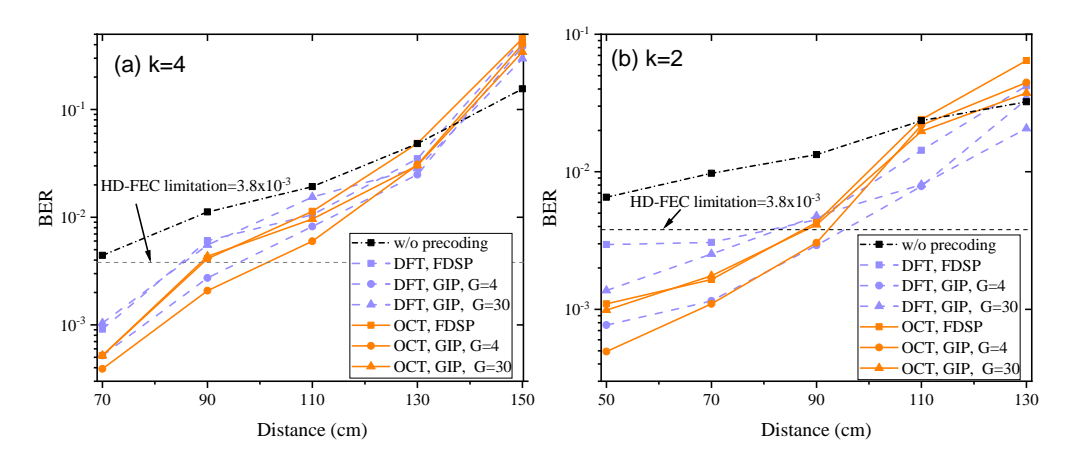


Fig. 6. Measured BER versus transmission distance for different schemes with (a) k = 4 and (b) k = 2.

In Fig. 7, we analyzed the SNR of data-carrying subcarriers using recovered constellation symbols for systems with k=2 and k=4, at transmission distances of 50cm and 70cm. All precoding schemes effectively balanced the SNR. The difference is the SNR over the low-frequency subcarrier of FDSP-MM-FBMC-IM with DFT in Fig. 7(a) exhibits significant fading exceeding 6 dB when k=2. This phenomenon, coupled with the partial high-frequency subcarrier fading in MM-FBMC-IM with k=2, is attributed to the interference caused by signal sidelobes from other subcarriers. Notably, GIP-MM-FBMC-IM shows superior resistance to out-of-band attenuation compared to FDSP-MM-FBMC-IM with DFT, diminishing signal sidelobes' impact from other subcarriers on specific signal main lobes. In Fig. 7(b), compared with DFT, OCT shows robust resistance to out-of-band attenuation, evidenced by the absence of significant SNR fading in FDSP-MM-FBMC-IM with OCT. In Fig. 7(c) and (d), the high overlap factor enhances the FBMC system's ability to resist out-of-band attenuation.

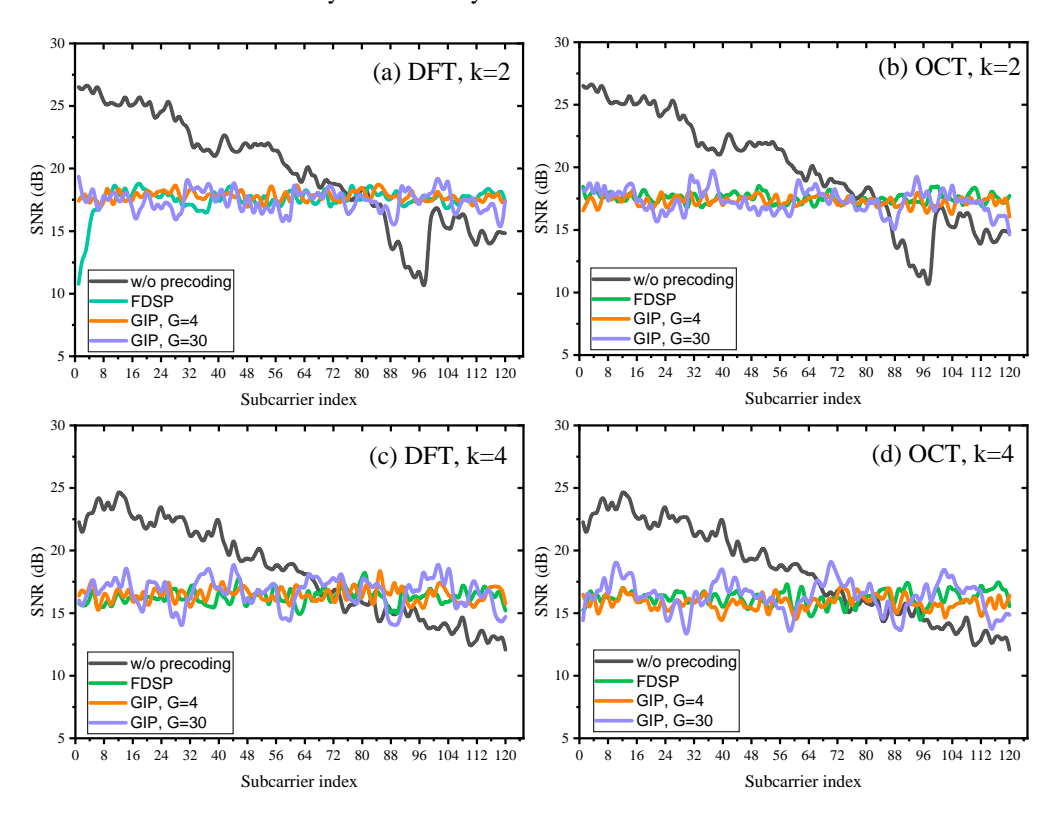


Fig. 7. Subcarrier index versus SNR for different schemes with (a) DFT, k = 2, (b) OCT, k = 2, (c) DFT, k = 4, and (d) OCT, k = 4.

In the final investigation, we explored the BER versus net bit rate for various schemes with a transmission distance of 90cm. The results of these experiments and part constellation diagrams are depicted in Fig. 8, where systems are configured with an overlap factor of k=4. Different net bit rates are achieved by adjusting the sampling rate using AWG. It is crucial to emphasize that the primary objective of this experiment is to conduct horizontal comparisons among different schemes to assess performance disparities. Numerous methods unrelated to the experimental purpose may significantly enhance the system's net bit rate. Regardless of the precoding matrix used, the GIP-MM-FBMC-IM with G=30 achieves performance equivalent to that of the FDSP-MM-FBMC-IM at the HD-FEC limitation. Furthermore, only GIP-MM-FBMC-IM with

G=4 achieved HD-FEC at a net bit rate exceeding 366 Mbit/s. Compared to FDSP-MM-FBMC-IM, the GIP-MM-FBMC-IM with G=4 improved the net bit rate by 22% and 18% at HD-FEC limitation when using DFT and OCT, respectively. Compared to systems without precoding, the GIP-MM-FBMC-IM with G=4 achieves an impressive maximum net bit rate improvement of 124%. However, beyond a net bit rate of 670 Mbit/s, precoding ceases to offer performance benefits and instead results in inferior performance compared to the system without precoding. In the case of a high net bit rate, it is evident that GIP-MM-FBMC-IM outperforms FDSP-MM-FBMC-IM. Furthermore, with the increase in G, the performance of GIP-MM-FBMC-IM gradually improves under conditions of elevated net bit rate. Therefore, the GIP scheme significantly improves the robustness of the MM-FBMC-IM compared to the FDSP scheme. It's noteworthy from the constellation diagrams that the system using the GIP exhibits the most convergence, while the system without precoding is the most scattered.

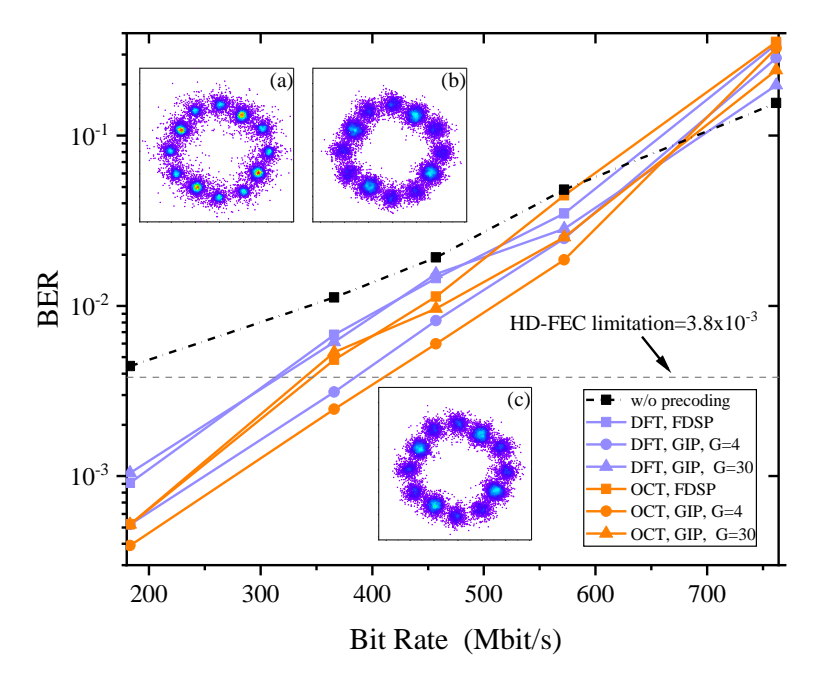


Fig. 8. The measured BER performance versus bit rate of different systems. Insets are the constellation diagrams for (a) without precoding, (b) FDSP with OCT, and (c) GIP with OCT at a net bit rate of 183 Mbit/s.

4. Conclusion

This paper presents the first application of MMIM in the FBMC-VLC system and proposes a novel low-complexity GIP scheme to address SNR imbalance impairments. In addition, we introduce a robust LCML detector that utilizes an optimized constellation design and mapping table. This detector achieves performance equivalent to the ML detector while maintaining the same complexity as the conventional LCML detector. Our simulation results demonstrate that GIP yields performance improvements of up to 0.8 dB over FDSP while reducing complexity by 75%. Moreover, the GIP scheme achieves similar BER performance with a remarkable complexity reduction of 96.7%. As a result, the GIP scheme effectively strikes a favorable balance between complexity and BER performance. Our experimental results confirm that precoding in the MM-FBMC-IM system leads to a remarkable bit rate improvement of over 124% under HD-FEC constraints. In particular, GIP exhibits exceptional resilience to out-of-band

attenuation, effectively mitigating the high-frequency subcarrier SNR attenuation observed in FDSP-MM-FBMC-IM with DFT. Even in scenarios with mild out-of-band attenuation, GIP offers a distinct advantage with G = 4, providing at least a 16% increase in transmission distance and a 22% increase in bit rate over FDSP.

Funding. National Natural Science Foundation of China (62271091); Natural Science Foundation of Hunan Province (2023JJ50197); Scientific Research Foundation of Hunan Provincial Education Department (22A0418, 23A0444).

Disclosures. The authors declare that there are no conflicts of interest related to this article.

Data availability. The data underlying the results presented in this paper are not publicly available at this time but may be obtained from the authors upon reasonable request.

References

- E. C. Strinati, S. Barbarossa, J. L. Gonzalez-Jimenez, et al., "6G: The next frontier: From holographic messaging to artificial intelligence using subterahertz and visible light communication," IEEE. Veh. Technol. Mag. 14(3), 42–50 (2019).
- 2. N. Chi, Y. Zhou, Y. Wei, *et al.*, "Visible light communication in 6G: Advances, challenges, and prospects," IEEE. Veh. Technol. Mag. **15**(4), 93–102 (2020).
- X. Zhu, C. X. Wang, J. Huang, et al., "A novel 3D non-stationary channel model for 6G indoor visible light communication systems," IEEE Trans. Wirel. Commun. 21(10), 8292–8307 (2022).
- L. Bariah, M. Elamassie, S. Muhaidat, et al., "Non-orthogonal multiple access-based underwater VLC systems in the presence of turbulence," IEEE. Photonics. J. 14(1), 1–7 (2022).
- S. Caputo, L. Mucchi, M. A. Umair, et al., "The Role of Bidirectional VLC Systems in Low-Latency 6G Vehicular Networks and Comparison with IEEE802. 11p and LTE/5G C-V2X," Sensors 22(22), 8618 (2022).
- C. H. Yeh, H. Y. Chen, C. W. Chow, et al., "Utilization of multi-band OFDM modulation to increase traffic rate of phosphor-LED wireless VLC," Opt. Express 23(2), 1133–1138 (2015).
- B. Lin, Q. Lai, Z. Ghassemlooy, et al., "A machine learning based signal demodulator in NOMA-VLC," J. Lightwave Technol. 39(10), 3081–3087 (2021).33
- K. A. Alaghbari, H. S. Lim, and T. Eltaif, "Compensation of chromatic dispersion and nonlinear phase noise using iterative soft decision feedback equalizer for coherent optical FBMC/OQAM systems," J. Lightwave Technol. 38(15), 3839–3849 (2020).
- M. Chen, A. Deng, L. Zhang, et al., "Precoding-enabled FBMC/OQAM for short-reach IMDD transmission," IEEE. Photonics Tech. Lett. 33(23), 1305–1308 (2021).
- J. Nadal, C. A. Nour, and A. Baghdadi, "Design and evaluation of a novel short prototype filter for FBMC/OQAM modulation," IEEE Access 6, 19610–19625 (2018).
- E. Başar, Ü. Aygölü, E. Panayıcı, et al., "Orthogonal frequency division multiplexing with index modulation," IEEE Trans. Signal Process. 61(22), 5536–5549 (2013).
- 12. J. Zhang, M. Zhao, J. Zhong, *et al.*, "Optimised index modulation for filter bank multicarrier system," IET Commun. 11(4), 459–467 (2017).
- 13. M. Wen, E. Basar, Q. Li, et al., "Multiple-mode orthogonal frequency division multiplexing with index modulation," IEEE Trans. Wirel. Commun. 65(9), 3892–3906 (2017).
- 14. T. Mao, Z. Wang, Q. Wang, et al., "Dual-mode index modulation aided OFDM," IEEE Access 5, 50-60 (2017).
- 15. M. Wen, Q. Li, E. Basar, *et al.*, "Generalized multiple-mode OFDM with index modulation," IEEE Trans. Wirel. Commun. **17**(10), 6531–6543 (2018).
- T. Ishihara and S. Sugiura, "Eigendecomposition-precoded faster-than-Nyquist signaling with optimal power allocation in frequency-selective fading channels," IEEE Trans. Wirel. Commun. 21(3), 1681–1693 (2022).
- C. Chen, Y. Nie, F. Ahmed, et al., "Constellation design of DFT-S-OFDM with dual-mode index modulation in VLC," Opt. Express 30(16), 28371–28384 (2022).
- H. Wen, H. Chen, Q. Chen, et al., "Performance enhanced dual-mode index modulation OFDM with OCT precoding in VLC systems," Opt. Commun. 530, 129191 (2023).
- 19. P. Chaki, T. Ishihara, and S. Sugiura, "Precoded filterbank multicarrier index modulation with non-orthogonal subcarrier spacing," IEEE Trans. Commun. 71(2), 700–713 (2023).
- Y. Liu, M. Chen, P. Liang, et al., "OCT-based partial data-carrying subcarriers precoding and ISFA-enabled DMT-VLC system," Chin. Opt. Lett. 21(2), 020602 (2023).
- T. Van Luong and Y. Ko, "Spread OFDM-IM with precoding matrix and low-complexity detection designs," IEEE Trans. Veh. Technol. 67(12), 11619–11626 (2018).